Article:
Liu, Z.-H., Nie, J., Wei, H.-L. et al. (2021) A newly designed VSC based current regulator for sensorless control of PMSM considering VSI nonlinearity. IEEE Journal of Emerging and Selected Topics in Power Electronics, 9 (4). pp. 4420-4431. ISSN: 2168-6777

https://doi.org/10.1109/jestpe.2020.3033037

Manuscript accepted for publication by *Journal of Emerging and Selected Topics in Power Electronics*

A Newly Designed VSC based Current Regulator for Sensorless Control of PMSM Considering VSI Nonlinearity

Zhao-Hua Liu, Jie Nie, Hua-Liang Wei, Lei Chen ,Xiao-Hua Li, Hong-Qiang Zhang

***Abstract*—A novel d-axis variable-structure control (VSC) current regulator for realizing fast and accurate sensorless control in the surface-mounted permanent magnet synchronous motor (SPMSM) is proposed in this paper. A switching-control law is employed to drive the plant's state trajectory onto a selected surface in the state space. Due to sign function is discontinuous and easy to cause chattering to the practical system, the sigmoid function is designed in this paper. The sensorless control performance under d-axis VSC current regulator is testified by sliding mode control (SMO) and model reference adaptive system (MRAS) method. In MRAS observer, the adaptive law of speed and resistance are designed so that resistance/speed/position can be estimated simultaneously, which can eliminate the influence of the resistance variations theoretically. In SMO observer, the back electromotive force observer is employed to estimate the PMSM speed and position so that the estimation can cover a relative low speed range because pure integration is not employed. Furthermore, the dead time compensation voltages (DTCV) strategy is employed to online estimate disturbance voltage in a feed-forward manner, which can improve the sensorless control performance of PMSM. Experimental results obtained from a SPMSM drive system are validate the superiority of the proposed d-axis VSC current regulator.**

***Index Terms*—Surface-mounted permanent magnet synchronous motor (SPMSM), estimation, speed-sensorless drive system, nonlinearities, dead-time compensation voltages (DTCV), variable-structure control (VSC), model reference adaptive system (MRAS).**

NOMENCLATURE[1]

A. General

R_r, R_s	Rotor, stator resistance.
P	Number of pole pairs.
J, B	Inertia and viscous friction.
T_e, T_l	Electrical and load torque.
θ_e	Electrical angle
L_m, L_s, L_r	Magnetizing, rotor, stator inductance.
E_{dc}	Dc link voltage.
φ	Rotor flux .
u, i	Stator voltage and current.
ω_m, ω_e	Mechanical and electrical angular velocity.
u_{dcom}, u_{qcom}	D/q axis dead-time voltage compensation.
V_{sat}, V_D	Saturation and diode forward voltage.
T_d, T_{on}, T_{off}	Dead time , turn-on/off delay time

B. Superscripts

$\wedge$	Estimated value.
$*$	Reference value.

C. Subscripts

(α, β)	Stator fixed coordinates.
(d, q)	Synchronous rotating coordinates.

I. INTRODUCTION

PERMANENT-MAGNET synchronous motors (PMSMs) have been widely used in various high-end equipment manufacturing industries due to their high torque per unit volume, high efficiency, large torque to inertia ratio, and excellent controllability [1]-[4]. There are two main techniques, namely, direct torque control (DTC) and field-oriented control (FOC) for position and speed control in the linear induction motors (LIM). However, the DTC type algorithms usually have the disadvantages of low speed stability, torque ripple and less robustness to parameter changes[5], [6]. Therefore, the FOC algorithm is often used in ac servo machine due to its efficiency for PMSM control and drive systems.

Unfortunately, in the conventional FOC control strategy, precise information of the realtime rotor position and speed is required to know so that the encoder, tachometer or other mechanical position sensors are needed in a gearbox with limited space [7]. Although accurate magnetic FOC could be achieved, the use of mechanical sensors reduces the reliability of the system, increases the motor volume and also makes the design of motor complicated, particularly in hostile environments [8]-[10]. Due to these considerations, the sensorless technology plays a very important role in PMSM to replace the mechanical sensors used to obtain the information of rotor speed and position, and the sensorless approach has a clear edge over the traditional vector-controlled drive [20].

Wide speed range capability and motor parameter insensitivity are very important in position sensorless vector control. Based on this, a variety of sensorless methods have

[1]Z.-H. Liu ,J. Nie, L. Chen ,X.-H Li and H.-Q Zhang are with the School of Information and Electrical Engineering, Hunan University of Science and Technology, Xiangtan 411201, China (e-mail: zhliu@hnu.edu.cn;amanjie@vip.qq.com;chenlei@hnust.edu.cn;lixiaohua_0227@163.com,hongniuok@tom.com).
H.-L. Wei is with the Department of Automatic Control and Systems Engineering, University of Sheffield, Sheffield S1 3JD, U.K. (e-mail: w.hualiang@sheffield.ac.uk).

been proposed, which can be generally divided into two categories: high-frequency signal injection methods, and back-EMF model-based methods. High-frequency signal injection methods have a good performance even in low-speed range and standstill operations. However, the main drawbacks of such methods lie in the unnecessary noise produced by the injected signals and they cannot be applied to surface-mounted PMSMs [16].

Unlike high-frequency signal injection methods, back-EMF model-based methods have no restriction regarding the structure of the PMSM and do not need extra high-frequency signal sources. Commonly used back-EMF model-based methods include sliding-mode-control (SMO) [11]-[16], model reference adaptive system (MRAS) [17]-[23] and extended Kalman filter (EKF) [24]-[26]. The design of the observers in these methods is very important because the quality of the estimation directly affects the performance of the whole control scheme.

Although the EKF algorithm is robust to the system noise, the advantages of this method are limited by the large amount of computation, the sensitivity of parameters, and the need for proper initialization [19]. In [25], a rotor position estimation algorithm based on the extended Kalman filter algorithm was proposed. However, only the experimental results at constant speed were considered, and it turned out that the error of the estimated rotor position was large.

Compared to EKF, the model-based method has been adopted for sensorless control in many applications as it is simple and easy to implement [26]. Rotor flux MRAS was first introduced by Schauder [19], and a lot of effort has been focused on improving its performance [8], [33]. In [33], a MRAS approach has been studied without considering the rotor position and the associated results were verified only in the Simulink. In [8], Zhen et.al. removed the integration element and stator leakage inductance so that MRAS can be performed in both lower and higher speed ranges. However, MRAS has a drawback in that it is sensitive to parameter change, especially to stator resistance [21]. Therefore, MRAS has been used extensively for combined rotor resistance and speed estimation in induction motors [17], [18]. In [17], an artificial neural network (ANN) technique is employed in MRAS for resistance estimation. In [18], MRAS wasemployed for estimating stator resistance and rotor flux linkage but the rotor speed was derived from phase-locked loop (PLL). However, no experiment was performed to test the robustness of the system when resistance varies with temperature.

Recently, a useful observer named SMO are attracting widespread attention because it is robust to noise and parameter uncertainties [11]. Different from the MRAS method, the SMO method always identifies the motor speed and position by using a back-EMF observer so that the estimation can cover a very low speed range, without using a pure integrator [35]. Therefore, the back EMF MRAS is believed to have superior performance. Nonetheless, phase compensation is still necessary due to the existence of LPF. Accordingly, some higher-order SMO methods are developed [13], [14]. In this paper, a low-pass filter and an additional position compensation of the rotor position are employed to reduce the chattering problem that commonly occurs in the conventional SMO. Theoretically speaking, for an ideal sliding mode motion with a sign function, the observer will not cause chattering due to infinity switching frequency of the system [4]. However, in the practical instruments, owing to the mechanical delay and other imperfects of the system, the ideal characteristic of infinity switching frequency cannot be achieved. Therefore, in this paper, we employ a sigmoid function to replace the sign function in the SMO observer design.

Nevertheless, no matter how reasonable the observer structure is, the dead time effect caused by the voltage source inverter (VSI) is inevitable. Especially at low speed, the control performance of the model based sensorless technique is poor due to the low back EMF, VSI nonlinearity, etc [37]. VSI nonlinearity is mainly caused by dead-time, turn-on/off delay and saturation voltage drop of the active switch, which cannot be eliminated. Such a nonlinearity will lead to voltage/current distortion, torque pulsations, resulting in mismatch between reference and actual voltage [28]. With the increase of switching frequency, the dead-time effect on VSI output voltage and current is also increasing. Therefore, neglecting the VSI nonlinearity will certainly affect the performance of sensorless control [27]. Bearing this in mind, VSI nonlinearity compensation techniques have been widely reported see e.g. [27]-[31]. In this paper, the mathematical model of VSI nonlinearity is given and the estimated disturbance voltage is added to the *d/q* current control loop in a feedforward manner [30].

As one of the PMSM high-performance control methods, the core of FOC technology is to control the excitation current i_d and torque current *iq,* respectively. The currents *id* and *iq* can be calculated from the three phase currents *ia*, *ib* and *ic* (which can be obtained by current sensors) by clark/park transformation. Traditionally, the scheme of two proportional-integral (PI) closed loop vector control is often employed in many real applications. However, the PI current regulator has a poor control performance for handling nonlinear disturbance, and such an issue cannot be solved simply by adjusting the parameters. Therefore, many advanced controllers have been developed based on neural networks, genetic algorithms, fuzzy logic systems, and wavelet-networks,- and were utilized to improve the performance of the control system [34], [38], [39]. In [34], Yasser et.al. employed variable-structure control to replace the traditional d-axis PI current regulator in the DTC strategy. However, sign function signal is discontinuous and easy to cause chattering to the system.

The main contributions of the paper are summarized as follows:

1) Different from existing regulators, a new d-axis VSC current regulator is designed, where the current can still be precisely controlled in the presence of external disturbance such as resistance variation.
2) To test the applicability and performance of the newly designed d-axis VSC current regulator, it is employed in both MRAS and SMO methods. In addition, the

resistance variation caused by temperature is considered in the experiment to testify the robustness.

3) The mathematical model of the VSI nonlinearity is proposed. A simple disturbance observer without any additional circuit and offline experimental measurement, disturbance voltages in the rotor reference *dq* frame caused by the dead time and nonideal switching characteristics of IGBT are estimated in an on-line manner and fed to *dq* current control loop in a feedforward manner for compensating the dead-time effects.

This paper is organized as follows. In Section II-A, we first analyze the PMSM mathematical model by considering the dead-time effect, and the equations of PMSM are presented. In Section II-B, the structure of the d-axis VSC current controller is proposed. In Section III, we employ two type of observers (i.e. MRAS and SMO) under d-axis PI/VSC current regulator to realize sensorless control of PMSM, respectively. The experimental results and detailed analysis are given in Section IV to show the superiority of the proposed d-axis VSC current regulator over the traditional d-axis PI current regulators. Finally, a brief conclusion is provided in Section V.

II. Modeling of PMSM

A. Modeling of SPMSM under the dead-time effect

Assume that the employed SPMSM has negligible magnetic saturation, iron losses and the eddy current loss, the dynamics of a PMSM in the rotor *d-q* coordinates can be described as follows:

$$\begin{cases} u_d = R_s i_d + L_d \dfrac{d}{dt} i_d - \omega_e L_q i_q \\ u_q = R_s i_q + L_q \dfrac{d}{dt} i_q + \omega_e L_d i_d + \omega_e \phi_f \end{cases} \tag{1}$$

$$\begin{cases} \varphi_q = L_q i_q + M_{qd} i_d + M_{qf} i_f \\ \varphi_d = L_d i_d + M_{dq} i_q + M_{df} i_f \end{cases} \tag{2}$$

where M_{dq} and M_{qd} are the mutual inductances between d/q axis, M_{df} and M_{qf} are the mutual inductances between d/q axis and permanent magnet.

$$\phi_s = \sqrt{\varphi_d^2 + \varphi_q^2} \tag{3}$$

$$\delta = \tan^{-1}\left(\varphi_q / \varphi_d\right) \tag{4}$$

Under the *d/q* two-phase rotationary reference frame, equivalent circuits of a three-phase PMSM are shown in Fig. 1

For the SPMSM, since the torque ripple is mainly caused by the flux harmonics in the permanent magnet, the effect of inductance harmonics can be neglected

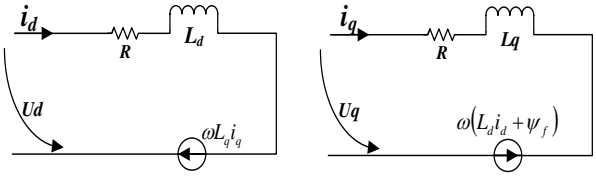

Fig. 1. Equivalent circuits of PMSM machine.

and the torque under i_d=0 control strategy can be characterized as:

$$T_e = 1.5 P \psi_f i_q \tag{5}$$

$$T_e - T_L = J\dot{\omega} + B\omega \tag{6}$$

Since the practical device has a finite switching time, a dead time should be considered in the PWM gate signals in order to prevent the simultaneous conduction of two switching devices in each leg of the inverter. Therefore, a top switch of one phase leg should be turned off before a bottom switch of the leg is turned on and vice versa. Although the dead time is very short, usually only a few microseconds, the effect of its cumulative effect over multiple cycles of the carrier waveform on the control performance of PMSM system cannot be ignored. Relevant parameters of the VSI are given in Table I.

TABLE I
SPECIFICATIONS OF EXPERIMENTAL SYSTEM

Dc link voltage 560 [V]	Switching period 166 [μs]
Dead-time 4 [μs]	Switching device IGBT
Turn-on time 0.8-2.0 [μs]	Turn-off time 2.0-2.9 [μs]
Saturation voltage 1.8-2.7 [V]	Diode forward voltage 2.2-2.3[V]

It is easy to analyze the dead-time effects from one phase leg of the inverter and extend the results to the other phase legs. Fig. 2 exhibits the basic configuration of one phase leg of the PWM inverter, where IGBTs are used as switching devices. During the dead-time period T_{dead}, both the main switching devices Q_1 and Q_4 in the same leg are turned off and the output voltage therefore depends on the direction of the phase current i_a When the phase current is positive/negative, the phase current flows through the bottom/top diode D_4 / D_1 during the dead-time period.

Fig. 3(a) shows the channel flow of A-phase current for positive direction (i_a >0). According to Fig. 3, considering the DTCV, (1) can be updated as follows:

$$\begin{cases} u_d^* + u_{d.com} = R_s i_d + L_d \dfrac{d}{dt} i_d - \omega_e L_q i_q + u_{d.dead} \\ u_q^* + u_{q.com} = R_s i_q + L_q \dfrac{d}{dt} i_q + \omega_e L_d i_d + \omega_e \varphi_f + u_{q.dead} \end{cases} \tag{7}$$

When $u_{d.dead}$ and $u_{q.dead}$ equal to the $u_{d.com}$ and $u_{q.com}$, respectively, the dead-time effect caused by VSI can be offset and compensated correctly. Furthermore, in the steady state, the disturbance voltages in the rotor reference frame can be represented as follows by employing the i_d=0 control strategy [30]:

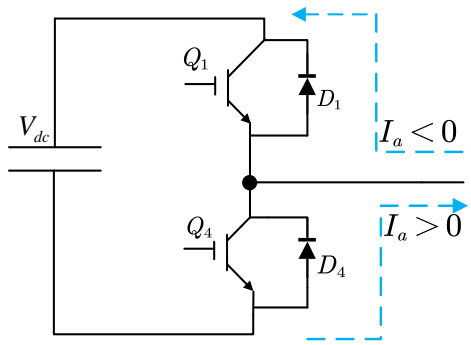

Fig. 2. Basic configuration of A phase leg of PWM inverter.

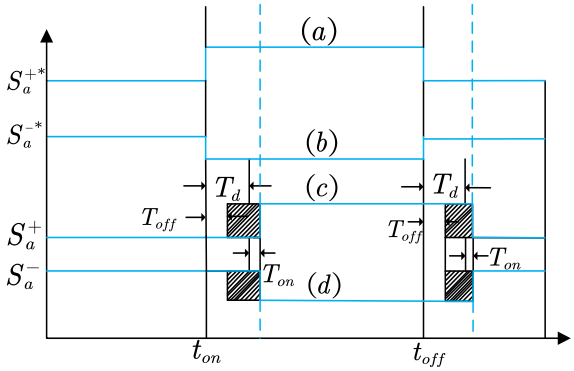

Fig. 3. A-phase bridge arm gate trigger pulse.

$$\begin{bmatrix} V_{q,\,\mathrm{dead}} \\ V_{d,\,\mathrm{dead}} \end{bmatrix} = V_{\mathrm{dead}} \cdot \mathbf{K}^r(\theta_r) \begin{bmatrix} \mathrm{sgn}\left(i_{\mathrm{qs}} \cos\theta_r\right) \\ \mathrm{sgn}\left(i_{\mathrm{qs}} \cos\left(\theta_r - \frac{2\pi}{3}\right)\right) \\ \mathrm{sgn}\left(i_{\mathrm{qs}} \cos\left(\theta_r + \frac{2\pi}{3}\right)\right) \end{bmatrix} \tag{8}$$

where $V_{\mathrm{dead}} = \frac{T_{\mathrm{dead}} + T_{\mathrm{on}} - T_{\mathrm{off}}}{T_s} \cdot \left(V_{\mathrm{dc}} - V_{\mathrm{sat}} + V_d\right) + \frac{V_{\mathrm{sat}} + V_d}{2}$ is the distorted voltage caused by switch on/off (T_{on}, T_{off}) and dead time (T_d) delay of PWM, and saturation voltage drop of the active switch (V_{sat}) and diode forward voltage(VD), respectively. $\mathbf{K}^r(\theta_r)$ is the rotation factor and can be derived from:

$$\mathbf{K}^r(\theta_r) = \frac{2}{3} \begin{bmatrix} \cos(\theta_r) & \cos\left(\theta_r - \frac{2\pi}{3}\right) & \cos\left(\theta_r + \frac{2\pi}{3}\right) \\ \sin(\theta_r) & \sin\left(\theta_r - \frac{2\pi}{3}\right) & \sin\left(\theta_r + \frac{2\pi}{3}\right) \end{bmatrix} \tag{9}$$

The $V_{q,dead}$ and $V_{d,dead}$ waveforms are shown in Fig. 16(c). It can be seen that $V_{q,dead}$ is larger than $V_{d,dead}$. Therefore, ignoring VSI nonlinearity has a great impact on the sensorless control.

B. The design of d-axis VSC current regulator

In the design of the d-axis current regulator, the main objective is to realize fast and accurate flux control ($i_d = 0$ control). A switching-control law is employed to drive the plant's state trajectory onto a selected surface in the state space (sliding surface). The mathematical model of the d-axis current regulator can be designed as:

$$S_{id} = \varepsilon_{id} + c_{id}\dot{\varepsilon}_{id} \tag{10}$$

where $\varepsilon_{id} = i^*_d - i_d$ is the d-axis current error , C_{id} is the coefficients of the sliding surface

In the sliding mode, it is required to restrict the controlled states onto their corresponding sliding surfaces. This is exclusively governed by $S = \dot{S} = 0$. Under this condition, the equivalent dynamics can be described as:

$$\varepsilon_{id} = -c_{id}\dot{\varepsilon}_{id} \tag{11}$$

The sliding-surface coefficients can be chosen to achieve the required dynamic performance on the

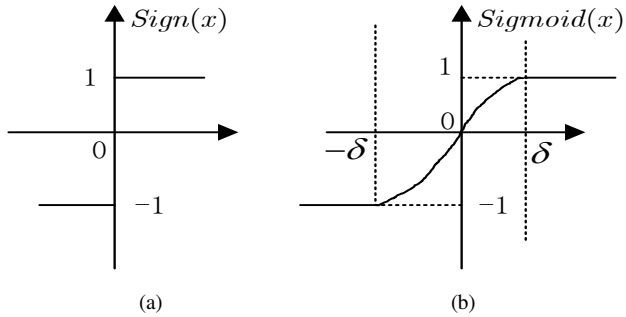

Fig. 4. Switching function employed in d-axis VSC (a) sign Function, (b) sigmoid function.

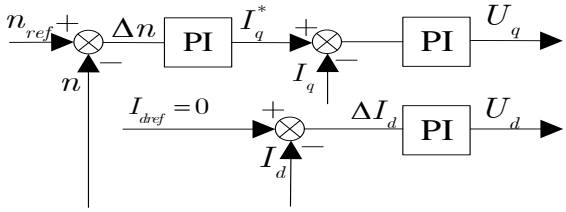

Fig. 5. Block diagram of the traditional two closed loop vector control.

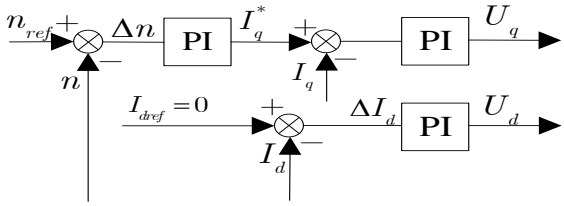

Fig. 6. Block diagram of the newly designed two closed loop.

control error without imposing stresses on the electrical and mechanical subsystems of the drive system.

Based on (10), the following control inputs are employed:

$$u_d^* = K_{i1}\,\mathrm{sgn}\left(S_{id}\right) + K_{i2}\int_0^t \mathrm{sgn}\left(S_{id}\right)dt \tag{12}$$

where K_{i1}, K_{i2} are the gains of the control input, $\mathrm{sgn}(\bullet)$ is the sign function and the symbols "*"denotes the reference value.

In order to reduce the chattering effect and to increase the degrees of freedom in tuning the controller, we employ the sigmoid function to replace the sign function as shown in Fig.4. Therefore, (10) and (12) can be updated as:

$$\begin{aligned} u_d^* &= K_{i1}Fal\left(S_{id}\right) + K_{i2}\int_0^t Fal\left(S_{id}\right)dt \\ S_{id} &= \varepsilon_{id} + c_{id}\dot{\varepsilon}_{id} \end{aligned} \tag{13}$$

where

$$Fal(s,\tau,\delta) = \begin{cases} |s|^{\tau}\,\mathrm{sign}(s) & |s| \geqslant \delta \\ \dfrac{s}{\delta^{1-\tau}} & |s| < \delta \end{cases} \tag{14}$$

where δ is the thickness of boundary layer in the range of (0, 1); τ is a positive coefficient in the range of [0, 1], which is employed to adjust the slope of the function.

The control law (13) restricts the system state onto the surface S in the sliding mode. Moreover, the control law produces a switching excitation signal controlled by K_{i1} superimposed by the slow-motion integral of the switching signal, which is controlled by K_{i2}. This hybrid control law gives more degrees of freedom to achieve adequate control performance with enough robustness and reduced chattering.

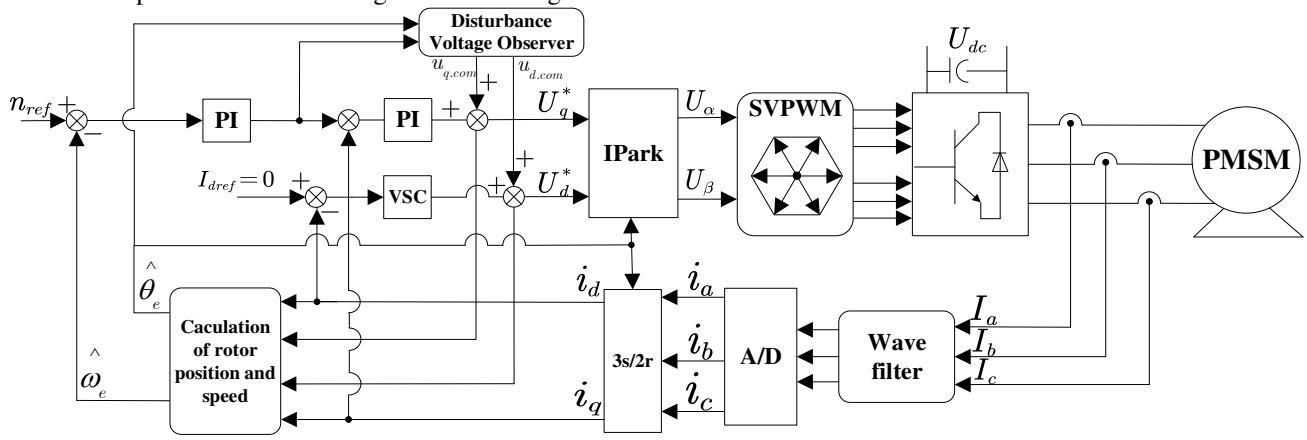

Fig. 7. Whole sensorless control system diagram with the proposed d-axis current regulator and VSI nonlinearity compensation

Usually, the VSC strategy needs the control law gains to be large enough to realize the rejection of wideband-disturbance. Specifically, the switching gain K_{i1} has to be large enough to ensure that the stability condition $\dot{S}S \le 0$ is satisfied.

The overall schematic diagram of the proposed rotor speed estimator, including the speed/rotor position estimator, and the disturbance voltage compensation, is shown in the Fig. 7.

III. Position And Speed Estimation

A. Mathematical models of the MRAS observer based on d-axis VSC current regulator

A MRAS observer is employed to estimate the rotor speed and the position of PMSM. Such an observer is comprised of two models, namely, the reference model and the adaptive model. All the information in the reference model is known, while the adaptive model contains unknown parameters that need to be identified from measurement; the output of the two models, however, has the same physical meaning.

In this paper, the adaptation algorithm is based on Popov hyperstability theory, which has been theoretically verified and the verification process can be found in [36]. According to the formula used in the full-order flux observer with speed adaptation, the speed tuning error signal ε can be computed as:

$$\varepsilon = \left(K_p + \frac{K_i}{S}\right)\left[i_d\hat{i}_q - i_q\hat{i}_d - \frac{\varphi_f}{L}\left(i_q - \hat{i}_q\right)\right] + \hat{\omega}_e(0) \qquad (15)$$

A PI controller is used to minimize this error, which in turn generates the estimated speed at its output

$$\hat{\omega}_e = \left(K_p + \frac{K_i}{S}\right)\varepsilon \qquad (16)$$

The resistance estimation formula can be written as:

$$\hat{R}_s = -\left(K_{pi} + \frac{K_{ii}}{p}\right)\left[\left(i_q - \hat{i}_q\right)\hat{i}_q + \left(i_d - \hat{i}_d\right)\hat{i}_d\right] \qquad (17)$$

The identification equation of rotor position follows:

$$\hat{\theta} = \int \hat{\omega}_e \qquad (18)$$

The symbols '$\wedge$' denotes the estimated value and the block diagram of the MRAS observer shown in Fig. 8.

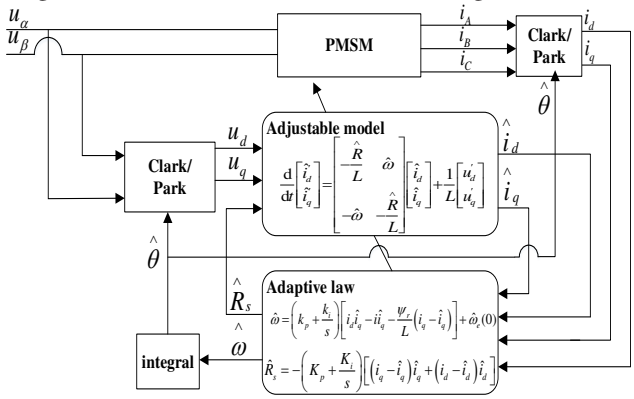

Fig. 8. Basic configuration of the MRAS scheme for estimating the speed and angular simultaneously.

B. Models of the SMO observer based on d-axis VSC current regulator

The current state equations of a motor in α/β two - phase stationary coordinate system are given as:

$$\begin{cases} \dfrac{di_\alpha}{dt} = -\dfrac{R_s}{L_s}i_\alpha + \dfrac{1}{L_s}u_\alpha - \dfrac{1}{L_s}e_\alpha \\ \dfrac{di_\beta}{dt} = -\dfrac{R_s}{L_s}i_\beta + \dfrac{1}{L_s}u_\beta - \dfrac{1}{L_s}e_\beta \end{cases} \qquad (19)$$

$$\begin{bmatrix} i_\alpha \\ i_\beta \end{bmatrix} = \sqrt{\frac{2}{3}}\begin{bmatrix} 1 & -\frac{1}{2} & -\frac{1}{2} \\ 0 & \frac{\sqrt{3}}{2} & -\frac{\sqrt{3}}{2} \end{bmatrix}\begin{bmatrix} i_A \\ i_B \\ i_C \end{bmatrix} \qquad (20)$$

The equations of BEMF are derived from

$$\begin{cases} e_\alpha = -\varphi_f \omega \sin\theta \\ e_\beta = \varphi_f \omega \cos\theta \end{cases} \tag{21}$$

According to the basic principle of SMC structure and the associated low pass filter (see Eq.(24)), we define the SMO switching function as:

$$s(x) = \begin{bmatrix} \hat{i}_\alpha - i_\alpha \\ \hat{i}_\beta - i_\beta \end{bmatrix} \tag{22}$$

The sliding-mode current observer is constructed as follows:

$$\begin{cases} \dfrac{d\hat{i}_\alpha}{dt} = -\dfrac{R_s}{L_s}\hat{i}_\alpha + \dfrac{1}{L_s}u_\alpha - \dfrac{k_s}{L_s} sign\left(\hat{i}_\alpha - i_\alpha\right) \\ \dfrac{d\hat{i}_\beta}{dt} = -\dfrac{R_s}{L_s}\hat{i}_\beta + \dfrac{1}{L_s}u_\beta - \dfrac{k_s}{L_s} sign\left(\hat{i}_\beta - i_\beta\right) \end{cases} \tag{23}$$

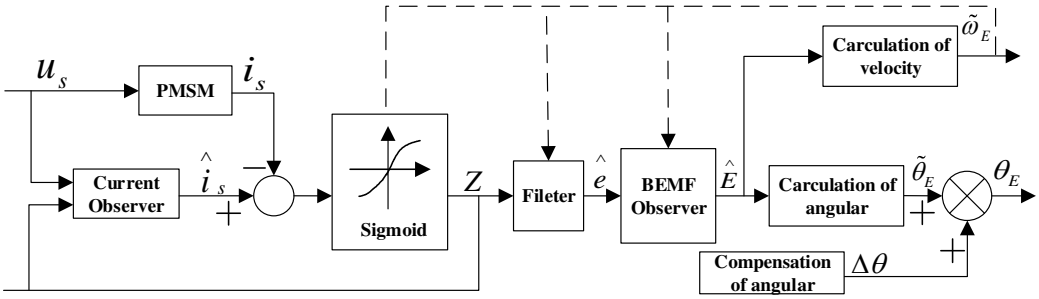

Fig. 9. Block diagram of the improved SMO scheme for estimate speed and position synchronously.

The back electromotive force (BEMF) estimate values are:

$$\begin{cases} z_\alpha = k_s \operatorname{sign}\left(\hat{i}_\alpha - i_\alpha\right) \\ z_\beta = k_s \operatorname{sign}\left(\hat{i}_\beta - i_\beta\right) \end{cases} \tag{24}$$

where K_s is the SM observer switching gain, its value must be large enough to satisfy the accessibility and existence of SMO. But large gain will increase the chattering noise and cause unnecessary estimation errors, so it needs to satisfy the following relationship:

$$k_s > \max\left(\left|e_\alpha\right|, \left|e_\beta\right|\right) \tag{25}$$

Due to the high frequency switching function, the output BEMF is also a high frequency discontinuous signal, which has some distortion and cannot be directly used to calculate the rotor position and speed. Therefore, it is necessary to introduce a low pass filter with sufficient cutoff frequency to remove the higher harmonics. The low-pass filter model is:

$$\begin{cases} \dfrac{d\hat{e}_\alpha}{dt} = -\omega_c\left(\hat{e}_\alpha - z_\alpha\right) \\ \dfrac{d\hat{e}_\beta}{dt} = -\omega_c\left(\hat{e}_\beta - z_\beta\right) \end{cases} \tag{26}$$

where ω_c is the cut-off frequency of the low-pass filter, expressed in terms of transfer functions

$$\begin{cases} \hat{e}_\alpha = \dfrac{\omega_c}{s}\left(z_\alpha - \hat{e}_\alpha\right) \\ \hat{e}_\beta = \dfrac{\omega_c}{s}\left(z_\beta - \hat{e}_\beta\right) \end{cases} \tag{27}$$

According to (20) and (26), we can know that rotor position information can be extracted from BEMF:

$$\tilde{\theta}_E = -\arctan\frac{\hat{e}_\alpha}{\hat{e}_\beta} \tag{28}$$

Because the first order low-pass filter is employed to filter the estimated BEMF, the rotor position should be compensated. The delayed phase is compensated by the cut-off frequency of the low-pass filter and the angular frequency of the input signal, as shown below:

$$\Delta\theta = \arctan\frac{\omega}{\omega_c} \tag{29}$$

where ω is the frequency of the input signal. Therefore, motor rotor position information can be expressed by the following equation:

$$\hat{\theta}_E = \tilde{\theta}_E + \Delta\theta = \arctan\frac{\hat{e}_\alpha}{\hat{e}_\beta} + \arctan\frac{\omega}{\omega_c} \tag{30}$$

The rotor speed can be obtained by differentiating the rotor position equation. However, differential function may reduce the dynamic performance of the system. Since the BEMF contains the information of speed, it is generally used to extract the speed information. According to (21), the rotor speed of the motor can be obtained as:

$$\begin{aligned} e &= \sqrt{\hat{e}_\alpha^2 + \hat{e}_\beta^2} \\ &= \sqrt{\left[\psi_f \hat{\omega}\sin\theta\right]^2 + \left[\psi_f \hat{\omega}\cos\theta\right]^2} = \left|\psi_f \hat{\omega}\right| \end{aligned} \tag{31}$$

In addition, the operation performance of the rotor is studied when the it rotates in the positive direction, so the rotor speed of the motor is:

$$\hat{\omega} = \frac{\sqrt{\hat{e}_\alpha^2 + \hat{e}_\beta^2}}{\psi_f} \tag{32}$$

Because of the discontinuity of the sign function, the power function, instead of the sign function, is used as the switching function in this paper, making the SMO switching function have switching characteristics and also can effectively reduce the discontinuity and chattering effect. According to the sigmoid function (14), (23) and (24) can be updated as:

$$\begin{cases} \dfrac{d\hat{i}_\alpha}{dt} = -\dfrac{R_s}{L_s}\hat{i}_\alpha + \dfrac{1}{L_s}u_\alpha - \dfrac{k_s}{L_s} Fal\left(\hat{i}_\alpha - i_\alpha\right) \\ \dfrac{d\hat{i}_\beta}{dt} = -\dfrac{R_s}{L_s}\hat{i}_\beta + \dfrac{1}{L_s}u_\beta - \dfrac{k_s}{L_s} Fal\left(\hat{i}_\beta - i_\beta\right) \end{cases} \tag{33}$$

Regulator/Observer	Gains
Speed regulator	K_p =0.24; K_i =1.23
PI current regulator	K_p =58.8; K_i =0.73
D-axis VSC current regulator	K_p =1.2; K_i =1; δ =0.5; τ =0.9; C_{id} =0.02.
MRAS observer for speed estimation	K_p =10.8; K_i =0.82
MRAS observer for resistance tracking	K_p =0.03; K_i =0.0015
SMO observer	K_s =0.36; δ =0.9; τ =1.0

$$\begin{cases} z_\alpha = k_s Fal\left(\hat{i}_\alpha - i_\alpha\right) \\ z_\beta = k_s Fal\left(\hat{i}_\beta - i_\beta\right) \end{cases} \quad (34)$$

Note that the coefficient K_s can affect the respond speed and a large K_s may make the system unstable. The block diagram of SMO observer is shown in the Fig. 9.

IV. Experimental Results And Discussions

A. Configuration of the Experimental System

In this section, to evaluate the control performance of the proposed d-axis VSC current regulator, the experimental results for sensorless control of PMSM are reported. Simulations are carried out in MATLAB/Simulink and the sampling frequency is 11.5 kHz. The experimental setup is given in Fig. 10 and the prototype machine design parameters are given in TABLE II. In all the tests, the

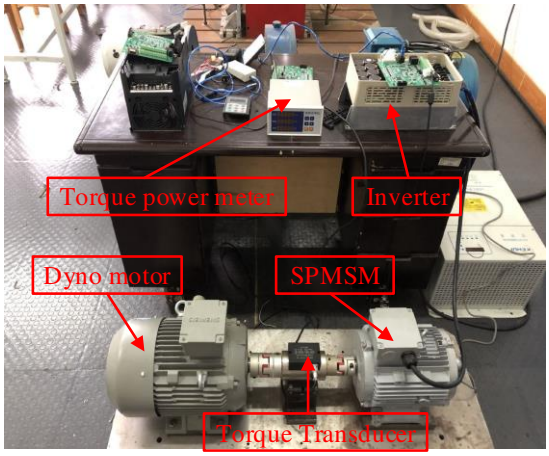

Fig. 10. The used prototype PMSM.

estimated speed is fed back to the speed control loop. To testify robustness of the system, the resistance variation is considered in the experiment. The gains used for the tuning of the PI regulator and observer is given in TABLE III.

TABLE II
DESIGNE PARAMETERS OF THE SPMSM

Machine	Parameters
Rated Speed	3000rpm
Rated current	4A
DC link voltage	311V
Nominal terminal wire resistance	0.043 Ω
Nominal self inductance	2.91mH
Nominal mutual inductance	-0.330mH
Nominal *d*-axis inductance	15.86mH
Nominal *q*-axis inductance	15.86mH
Nominal amplitude of flux induced by magnets	79mWb
Number of pole pairs	4
Nominal phase resistance(T=25℃)	1.204 Ω
Nominal moment of inertia	0.8e-5 kg.m^2

Note: Nominal values are measured.

TABLE III
GAINS USED FOR REGULATOR AND OBSERVER

B. Experimental schemes and results analysis

In order to show the superiority of the proposed d-axis VSC current regulator based on DTCV strategy, the following four schemes are introduced and investigated in the experiment.

1) *Sensorless control at variable speed with DTCV based on MARS observer at 1.204Ω:* Under this condition, set a step speed command but the stator resistance remains 1.204 Ω . An MRAS observer has been employed for estimating the rotor speed using (15). The experimental result using the MRAS observer based on d-axis PI/VSC current regulator is shown in Fig. 11 and Fig. 12. At first, the rotor speed is 100rpm, which suddenly changes to 50rpm at the 1s and return to 100rpm in the 2s. The rotor speed changes periodically at the time of 3s and 4s. Fig. 11(a) shows the measured and estimated speed under d-axis PI current regulator. The dashed line represents the measured speed, and the solid line represents the estimated speed. The actual rotor speed reaches the command in about 0.3s. It can be seen clearly that the estimated speed can quickly track the measured speed. To further validate the superiority of the proposed d-axis VSC current regulator, Fig. 11(b) exhibits the experimental result under d-axis VSC current regulator. Compared with Fig. 11(a), it has a faster convergence speed, smaller steady state error and smaller overshoot. The experimental results at speed variations ± 50 and ± 100 rpm during 10 seconds with rated load 20N are shown in Fig. 12. As shown in Fig. 12(c) and (d), it has a smaller steady state error as shown and a smaller overshoot under d-axis VSC current regulator. The experimental results show that MRAS observer has a good sensorless performance, and the control accuracy is better at d-axis VSC current regulator.

2) *Sensorless control at variable speed with DTCV based on SMO observer at 1.204Ω:* Under this condition, the reference speed is set to be the same as that of Scheme I and the experimental results using SMO observer under d-axis PI/VSC regulator are shown in Fig. 13(a)-(c). From Fig. 13(a), the actual rotor speed ramps up from standstill to 100 r/min in about 0.58s. Compared with the results of MRAS observer as shown in Fig. 12(a), no overshoot occurs in Fig. 13(a). The estimated speed also shows a faster convergence rate obtained by d-axis VSC current regulator and a smaller measured error as shown in Fig. 13(c). The tracking error is less than 0.1% under d-axis VSC current regulator. The estimated and the corresponding actual rotor position are given in Fig. 13(c), where it can be seen that the measured error is relatively small. The experimental results show that the sensorless control for SPMSM is good in this scheme and the performance is better at d-axis VSC current regulator.

3) *Sensorless control at constant speed with DTCV under resistance variation:* In the practical application, the stator resistance would increase when the temperature is rising. Therefore, stator resistance variation is considered as a disturbance and the speed command is set to 1000rpm. The MRAS estimator is employed for speed and resistance estimation using (15)-(17). The experimental results using MRAS observer are shown in Fig. 14(a)-(d). In Fig. 14(a), the dashed line represents the measured resistance. Note that the measured resistance means the change process of stator resistance which follows 1.204Ω (100%) → 1.806Ω (150%) → 1.204Ω (100%) → 0.8428Ω (70%) → 1.204Ω (100%). It can be seen that the estimated resistance under MRAS observer has a high accuracy. Fig. 14(c) exhibits the corresponding speed response. It can be seen that the speed undershoot and overshoot are smaller under d-axis VSC current regulator. In Fig. 15(a), the change process of the stator resistance (i.e. the measured resistance) follows 1.204Ω (100%) → 2.408Ω (200%) → 1.806Ω (150%) → 1.204Ω (100%) → 0.8428Ω (70%). From Fig. 15(b), it can be found

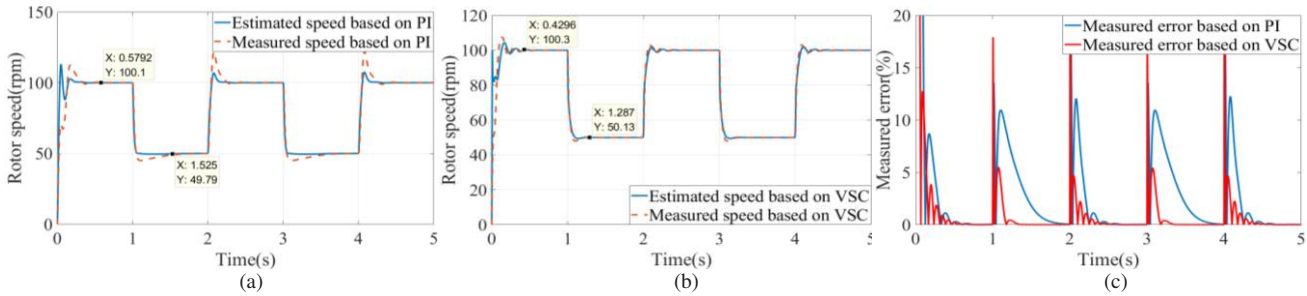

Fig. 11. Speed estimation using MRAS observer at 1.204 Ω . (a) Under d-axis PI current regulator; (b) Under d-axis VSC current regulator; (c) Measured error between d-axis PI/VSC method.

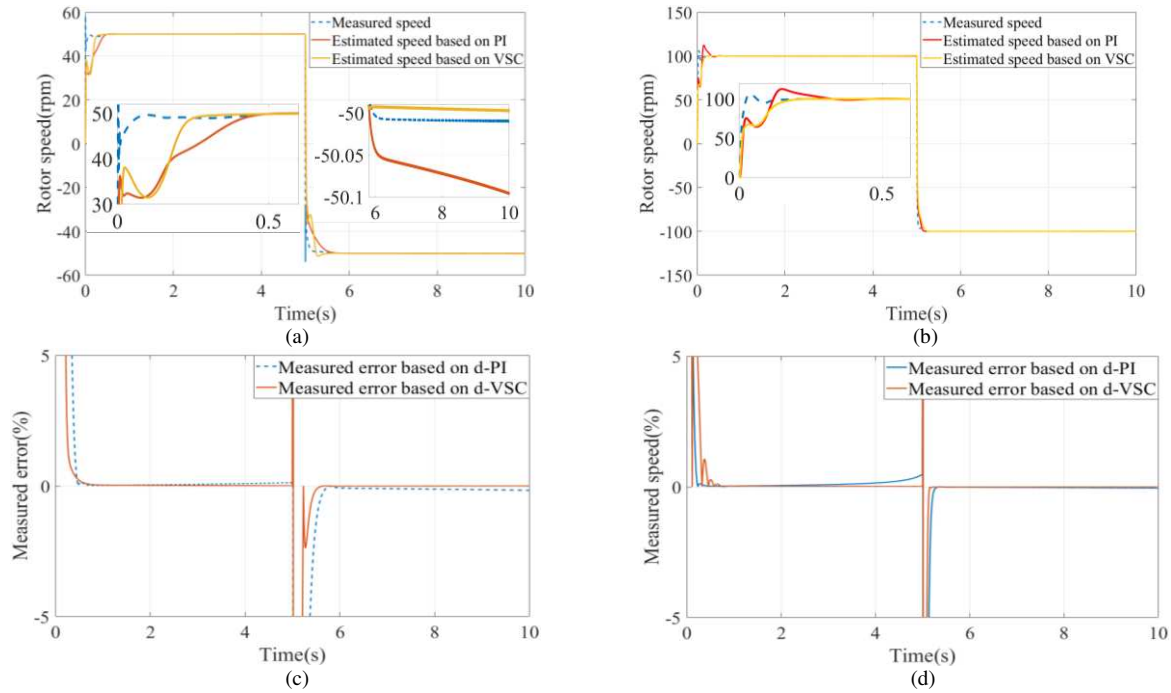

Fig. 12. Speed reversal estimation using MRAS observer at 1.204 Ω with rated load 20N. (a) 50rpm→-50rpm based on d-axis PI/VSC method; (b) 100rpm→-100rpm based on d-axis PI/VSC method; (c) Measured error of 50rpm→-50rpm; (d) Measured error of 100rpm→-100rpm.

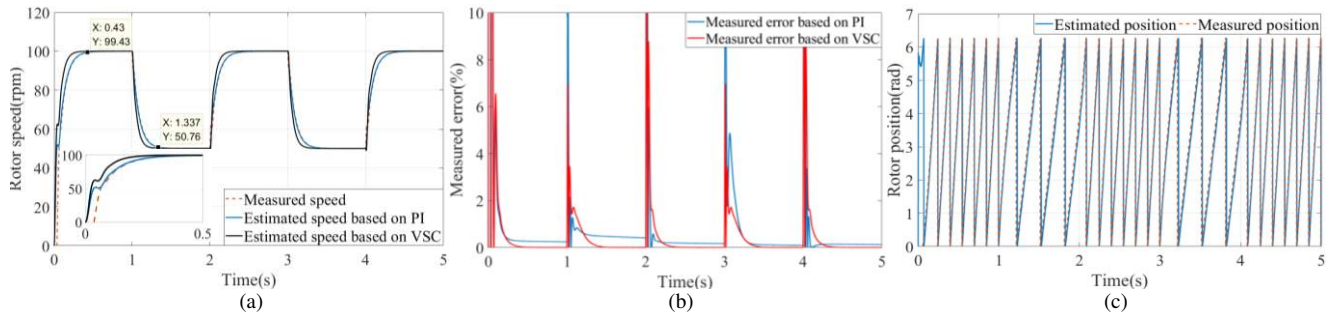

Fig. 13. Speed estimation using SMO observer at 1.204 Ω . (a) Under d-axis PI/VSC current regulator; (c) Comparison of the Measured error; (d) Estimated and actual rotor position.

that the measured error is less than 7.5% in the steady state. The corresponding speed response is shown in Fig. 15(c). These results show that the sensorless control performance for PMSM is good and robust in the MRAS observer at d-axis VSC current regulator. Furthermore, the comparison between online/no estimation of resistance is also carried out and the experimental result is shown in Fig. 14(d). It is obvious that the estimation accuracy of speed can be improved if resistance is online estimated.

The SMO observer for speed and rotor position using (27)-(32). The reference speed is set to 100rpm. The experiment is performed on d-axis PI/VSC current regulator for further demonstrating the superiority of the proposed d-axis VSC current regulator. The experimental results using SMO observer are shown in Fig. 14(e)-(g). In Fig. 14(e), the actual rotor speed reaches the command within about 0.2s/0.15s under d-axis PI/VSC current regulator. It is evident that the whole system has a good robustness to resistance variation. The estimated speed under the d-axis VSC current regulator has a shorter rise time and smaller

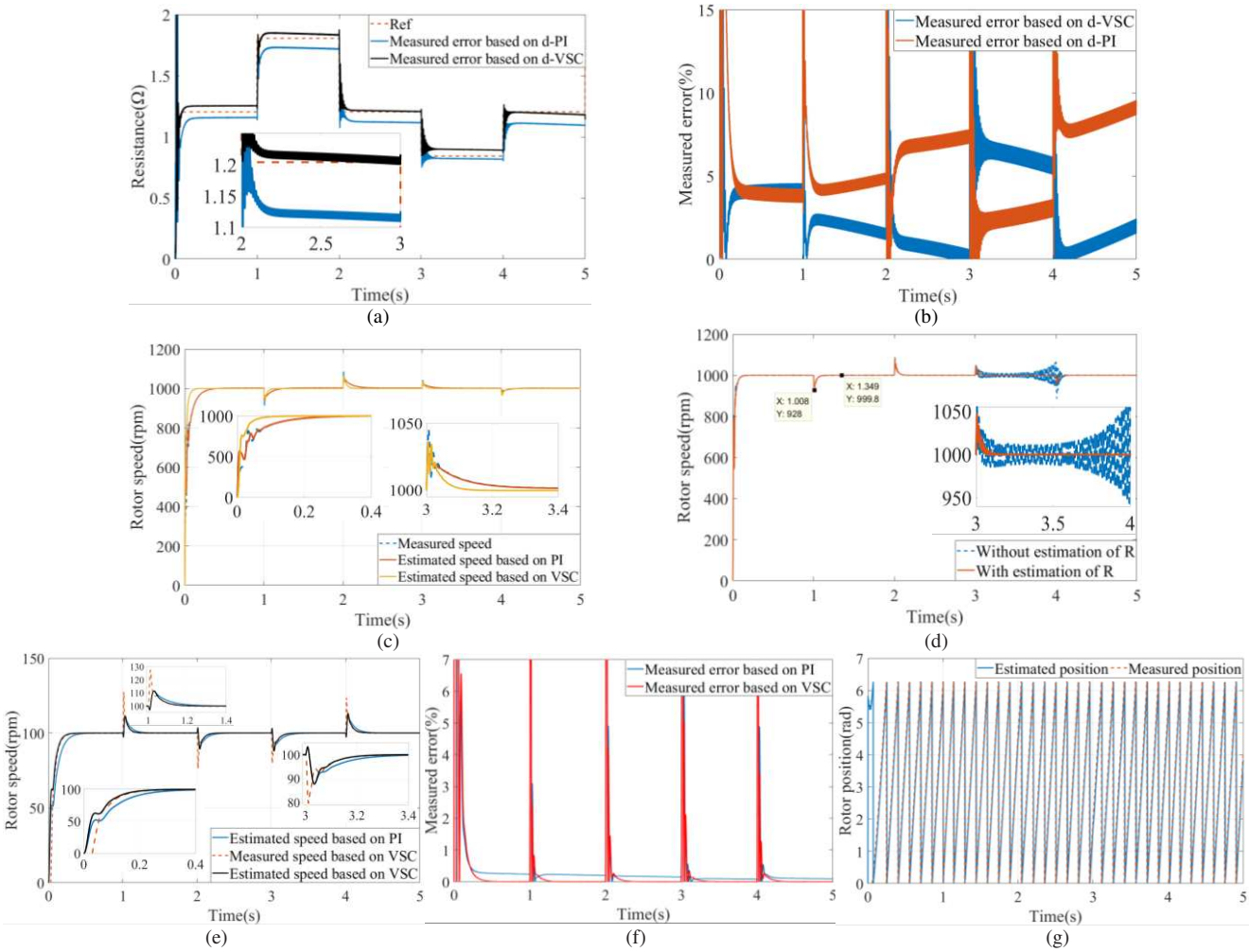

Fig. 14. Study on a big change of stator resistance(100%-150%-100%-150%-100%). (a) Estimated resistance using MRAS observer; (b) Measured error of resistance; (c) The estimated speed using MRAS observer at 1000rpm; (d) Estimated speed with/without resistance estimation under resistance variation; (e) The estimated speed using SMO observer at 100rpm; (f) Measured error of speed; (g) Estimated and actual rotor position using d-axis VSC regulator.

steady-state error compared to d-axis PI current regulator as shown in Fig. 14(f). It can be seen that the steady-state error is less than 0.3 % under the d-axis VSC current regulator. Furthermore, rotor position estimation are given In Fig. 14(g) and the measured error is also relative small. Although the first-order low-pass filtering can cause phase lag, the estimated rotor position is derived from back EMF and is compensate properly. Therefore, the sensorless control performance for SPMSM is good using SMO observer and the performance is better at d-axis VSC current regulator.

4) *Sensorless control and resistance tracking at constant speed considering DTCV based on MRAS observer:* Under this condition, the comparison of sensorless control between DTCV and without DTCV is shown in Fig. 16. Fig. 16(a) shows that the whole system without DTCV not only exhibits lower efficiency but also suffers usual speed overshoot and undershoot before reaching steady-state speed. The measured error of speed with DTCV is also smaller than that without DTCV. Resistance tracking is shown in Fig. 16(b). It can be seen that resistance can be more closely tracked with DTCV.

Simulation waveforms of *Dd* and *Dq* under i_d=0 control and speed command of 1000 rpm are shown in Fig. 16(c). It can be seen that *q*-axis DTCV V_q^{com} is a DC voltage with pulsation. On the other hand, *d*-axis DTCV V_d^{com} is an AC voltage.Finally, a detailed comparison table demonstrating both the qualitative and quantitative superiority of the proposed method over d-axis PI current regulator ispresented in Table IV.

V. Conclusion

An effective d-axis VSC current regulator for sensorless SPMSM drive considering VSI nonlinearity scheme is proposed for the first time in this paper. The proposed regulator can reduce or avoid the overshoot of rotor speed estimation and improve the performance of sensorless control. We investigated the performance of the sensorless control of the MRAS/SMO observers under the d-axis PI/VSC current regulator, respectively. Sensorless control and resistance tracking at variable speed with/without DTCV are also studied. The experimental results show that the proposed VSC current regulator has the following properties:

1) The MRAS observer has good sensorless control performance at low, medium or high speed and robust to resistance variation. MRAS observer can also track the resistance very quickly and the measured error is smaller under d-axis VSC current regulator.

2) The SMO observer has a faster convergence but the

Table IV A detailed comparison between d-axis PI and d-axis VSC regulator.

		Control Strategy							
D-axis control method		D-axis PI current regulator				D-axis VSC current regulator			
Evaluation index		Rise time	Overshoot	Undershoot	Error	Rise time	Overshoot	Undershoot	Error
Unit		Second(s)	Percent(%)	Percent(%)	Percent(%)	Second(s)	Percent(%)	Percent(%)	Percent(%)
Disturbance	Operating mode								
Resistance Unchanged (at 1.204 Ω)	50rpm~50rpm(MRAS)	0.76	0	0	0.07	0.54	0	0	0.01
	100rpm~100rpm(MRAS)	0.65	12.8	0.13	0.08	0.23	0.05	0	0.01
	100rpm~50rpm(SMO)	0.62	13.2	10.1	0.05	0.58	7.62	4.21	0.01
Resistance Variation (100%-150%-100%-150%-100%)	100rpm(SMO)	0.61	28.5	24.1	0.26	0.37	27.4	23.7	0.01
	1000rpm(MRAS)	0.65	0.21	6.21	0.04	0.27	0	5.03	0.02
Resistance Variation (100%-200%-150%-100%-70%)	100rpm(SMO)	0.54	11.7	1.02	0.26	0.48	11.4	0.71	0.01
	1000rpm(MRAS)	0.56	6.95	3.82	0.21	0.31	6.51	0.61	0.04
VSI nonlinearity		Without DTCV strategy				With DTCV strategy			
Resistance Variation (100%-150%-100%-150%-100%)	1000rpm(MRAS)	0.41	6.72	8.08	2.05	0.22	0	7.21	0.02
Parameter estimation		Without resistance estimation				With resistance estimation			
Resistance Variation (100%-150%-100%-150%-100%)	1000rpm(MRAS)	0.24	8.75	8.08	1.52	0.24	8.11	7.22	0.02
Resistance Variation (100%-200%-150%-100%-70%)		0.24	8.65	16.7	1.24	0.24	8.45	15.6	0.02

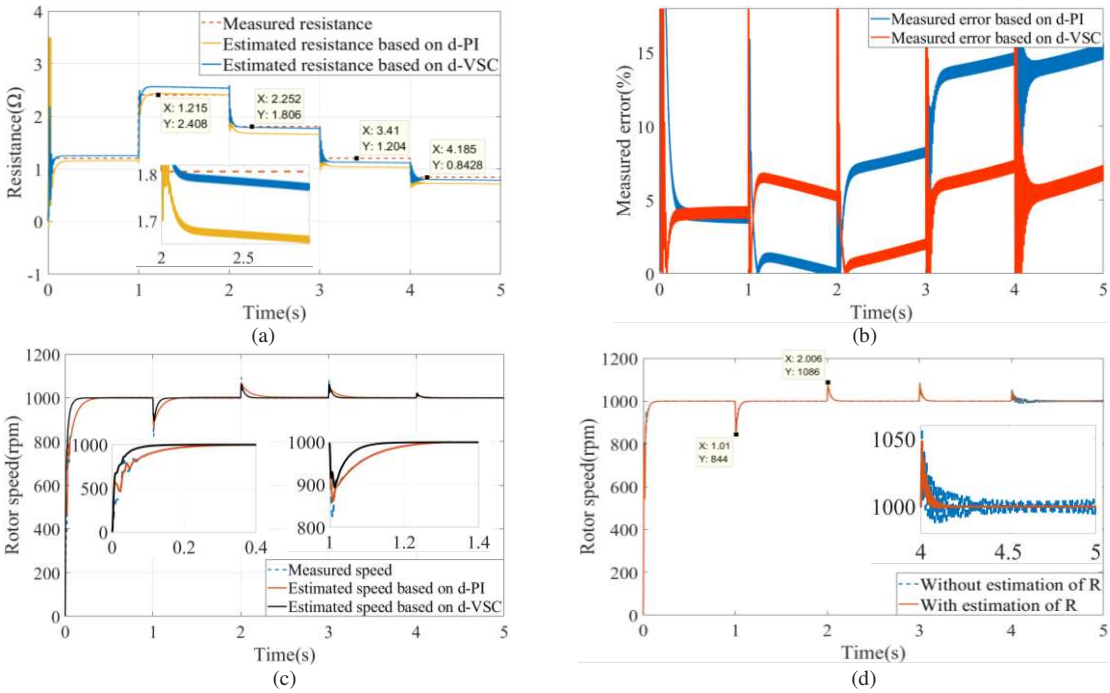

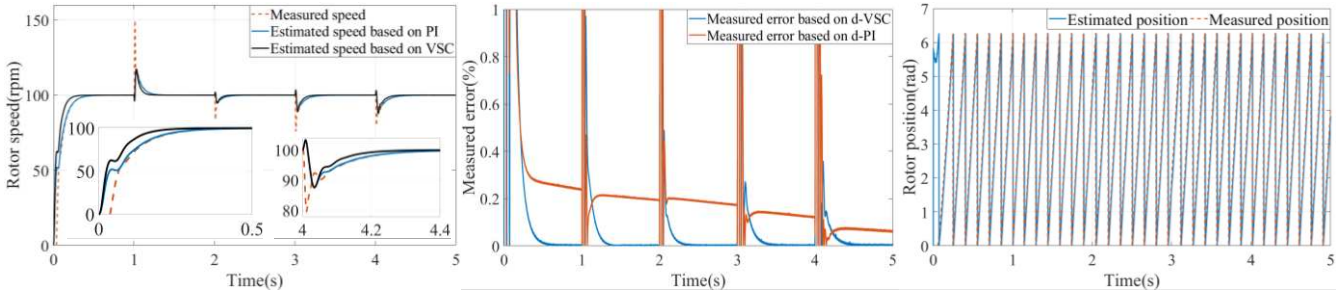

(e) (f) (g)

Fig. 15. Study on a big change of stator resistance using MRAS observer (100%-200%-150%-100%-70%). (a) Estimated and actual resistance; (b) Measured error of resistance; (c) The corresponding estimated speed; (d) Estimated speed with/without resistance estimation; (e) The estimated speed using SMO observer at 100rpm; (f) Measured error of speed; (g) Estimated and actual rotor position using d-axis VSC regulator.

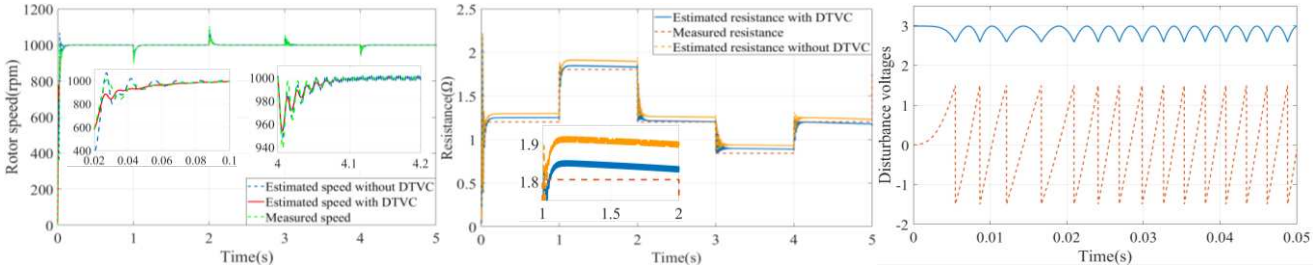

(a) (b) (c)

Fig. 16. Experimental results with/without DTCV at resistance variation(100%-150%-100%-150%-100%) using d-VSC regulator. (a) Speed estimation; (b) Resistance estimation; (c) Simulation waveforms of *Dd* and *Dq* under $i_d = 0$ control and speed command of 1000 rpm (Solid line: q-axis disturbance voltage $V_{q,dead}$, Dotted line: d-axis disturbance voltage $V_{d,dead}$).

steady-state error is larger than MRAS and the stator resistance can not be identified. Therefore, its overshoot and undershoot can be large compared to MRAS when resistance varies. In addition, better sensorless control performance can be obtained under d-axis VSC current controller.

3) The dynamic performance such as estimation accuracy of sensorless control and resistance tracking cab be improved if DTCV strategy is adopted.

REFERENCES

[1] P. Sun, Q. Ge, B. Zhang and X. Wang, "Sensorless Control Technique of PMSM Based on RLS On-Line Parameter Identification," 21st proceedings of *International Conference on Electrical Machines and Systems*, Jeju, 2018, pp. 1670-1673.

[2] K. Liu and Z. Q. Zhu, "Parameter estimation of PMSM for aiding PI regulator design of field oriented control," *2014 17th Int. Conf. Electrical Machines and Systems*, Hangzhou, 2014, pp. 2705-2711.

[3] J. Sopanen, V. Ruuskanen, J. Nerg, and J. Pyrhonen, "Dynamic torque analysis of a wind turbine drive train including a direct-driven permanentmagnet generator," *IEEE Trans. Ind. Electron*., vol. 58, no. 9, pp. 3859 – 3867, Sep. 2011.

[4] M. Comanescu, "Design and analysis of a sensorless sliding mode flux observer for induction motor drives," *2011 IEEE Int. Conf. Electrical Machines and Drives*, Niagara Falls, ON, 2011, pp. 569-574.

[5] S.J. Fattahi and A.A.Khayyat. Direct Torque Control of Brushless Doubly Fed Induction Machine, *International Journal of Control and Automation*. 3(4):21-32, 2010.

[6] Y. Wang, L. Geng, W. Hao and W. Xiao, "Control Method for Optimal Dynamic Performance of DTC-Based PMSM Drives," *IEEE Trans. Energy Convers*., vol. 33, no. 3, pp. 1285-1296, Sept. 2018.

[7] Yong Chen, Meng Li, Yu-wen Gao, Zhang-yong Chen, A sliding mode speed and position observer for a surface-mounted PMSM, *ISA Trans*, 2019; 87:17-27.

[8] A V R Teja, V Verma and C Chakraborty. "A New Formulation of Reactive-Power-Based Model Reference Adaptive System for Sensorless Induction Motor Drive," *IEEE Trans. Ind. Electron*, vol. 62, no. 11, pp. 6797-6808, Nov. 2015.

[9] C. M. Verrelli et al., "Speed Sensor Fault Tolerant PMSM Machines: From Position-Sensorless to Sensorless Control," *IEEE Trans. Ind. Appl*, vol. 55, no. 4, pp. 3946-3954, July-Aug. 2019.

[10] T. Boileau, N. Leboeuf, B. Nahid-Mobarakeh and F. Meibody-Tabar, "Online Identification of PMSM Parameters: Parameter Identifiability and Estimator Comparative Study," *IEEE Trans. Ind. Appl*, vol. 47, no. 4, pp. 1944-1957, July-Aug. 2011.

[11] K. Zhao et al., "Robust Model-Free Nonsingular Terminal Sliding Mode Control for PMSM Demagnetization Fault," *IEEE Access*, vol. 7, pp. 15737-15748, 2019.

[12] Z. Ma and X. Zhang, "FPGA Implementation of Sensorless Sliding Mode Observer With a Novel Rotation Direction Detection for PMSM Drives," *IEEE Access*, vol. 6, pp. 55528-55536, 2018.

[13] L. Zhao, J. Huang, H. Liu, B. Li, and W. Kong, "Second-order sliding mode observer with online parameter identification for sensorless induc tion motor drives," *IEEE Trans. Ind. Electron*., vol. 61, no. 10, pp. 5280 – 5289, Oct. 2014.

[14] D. Liang, J. Li and R. Qu, "Sensorless Control of Permanent Magnet Synchronous Machine Based on Second-Order Sliding-Mode Observer With Online Resistance Estimation," *IEEE Trans. Ind. Appl.*, vol. 53, no. 4, pp. 3672-3682, July-Aug. 2017.

[15] D. Bao, X. Pan, Y. Wang, X. Wang and K. Li, "Adaptive Synchronous-Frequency Tracking-Mode Observer for the Sensorless Control of a Surface PMSM," *IEEE Trans. Ind. Appl*., vol. 54, no. 6, pp. 6460-6471, Nov.-Dec. 2018.

[16] M. S. Islam, I. Husain, R. J. Veillette and C. Batur, "Design and performance analysis of sliding-mode observers for sensorless operation of switched reluctance motors," *IEEE Trans. Control Syst. Technol*., vol. 11, no. 3, pp. 383-389, May 2003.

[17] S. E. Rezgui, S. Legrioui, A. Mehdi and H. Benalla, "Robust IM control with MRAS-based speed and parameters estimation with ANN using exponential reaching law," *2014 International Conference on Control, Decision and Information Technologies (CoDIT)*, Metz, 2014, pp. 477-482.

[18] O. C. Kivanc and S. B. Ozturk, "Sensorless PMSM Drive Based on Stator Feedforward Voltage Estimation Improved With MRAS Multiparameter Estimation," *IEEE/ASME Trans Mechatronics*, vol. 23, no. 3, pp. 1326-1337, June 2018.

[19] C. Schauder, “Adaptive speed identification for vector control of induction motors without rotational transducers,” *IEEE Trans. Ind. Appl*., vol. 28, no. 5, pp. 1054 – 1061, Sep./Oct. 1992.

[20] I. Benlaloui, S. Drid, L. Chrifi-Alaoui and M. Ouriagli, "Implementation of a New MRAS Speed Sensorless Vector Control of Induction Machine," *IEEE Trans. Energy Convers*, vol. 30, no. 2, pp. 588-595, June 2015.

[21] Hag-Wone Kim, Myung-Joong Youn, Kwan-Yuhl Cho and Hyun-Soo Kim, "Nonlinearity estimation and compensation of PWM VSI for PMSM under resistance and flux linkage uncertainty," *IEEE Trans. Contr. Syst. Technol*., vol. 14, no. 4, pp. 589-601, July 2006..

[22] M. Comanescu, “An MRAS-type estimator for the speed, flux magnitude and rotor flux angle of the induction motor using sliding mode,” *Proc. Int. SPEEDAM*, Jun. 2014, pp. 719–724.

[23] Y. B. Zbede, S. M. Gadoue and D. J. Atkinson, "Model Predictive MRAS Estimator for Sensorless Induction Motor Drives," *IEEE Trans Ind Electron*, vol. 63, no. 6, pp. 3511-3521, June 2016.

[24] G. Tian, Y. Yan, W. Jun, Z. Y. Ru and Z. X. Peng, "Rotor Position Estimation of Sensorless PMSM Based on Extented Kalman Filter," *IEEE Int. Conf. on Mechatronics*, Robotics and Automation, Hefei, 2018, pp. 12-16.

[25] R A Walambe and V A Joshi. Closed Loop Stability of a PMSM-EKF Controller-Observer Structure, *IFAC-PapersOnLine*, vol. 51, Issue 1,2018,Pages 249-254.

[26] D. Zhang and J. G. Jiang, "Sensorless control of PMSM for DC micro-grid flywheel energy storage based on EKF," *The Journal of Engineering*, vol. 2019, no. 16, pp. 1227-1231, 3 2019.

[27] G. Feng, C. Lai, K. Mukherjee and N. C. Kar, "Current Injection-Based Online Parameter and VSI Nonlinearity Estimation for PMSM Drives Using Current and Voltage DC Components," *IEEE Trans. Transport. Electrific.*, vol. 2, no. 2, pp. 119-128, June 2016.

[28] H.-S. Kim, K.-H. Kim, and M.-J. Youn, “On-line dead-time compensation method based on time delay control,” *IEEE Trans. Control Syst. Technol*., vol. 11, no. 2, pp. 279 – 285, Mar. 2003.

[29] Julio E. Normey-Rico, Rodolfo C.C. Flesch, Tito L.M. Santos,Unified dead-time compensation structure for SISO processes with multiple dead times, *ISA Trans*, 2014; 53:1865-1872.

[30] Hyun-Soo Kim, Hyung-Tae Moon and Myung-Joong Youn, "On-line dead-time compensation method using disturbance observer," *IEEE Trans Power Electron*, vol. 18, no. 6, pp. 1336-1345, Nov. 2003.

[31] He Zhengyi and Ji Xuewu, "A new inverter compensation strategy based on adjusting dead-time on-line," *IEEE Int. Symposium on Ind. Electron*., Cambridge, 2008, pp. 768-773.

[32] X. Zhang and Z. Li, "Sliding-Mode Observer-Based Mechanical Parameter Estimation for Permanent Magnet Synchronous Motor," *IEEE Trans. Power Electron.*, vol. 31, no. 8, pp. 5732-5745, Aug. 2016.

[33] M. Manohar and S. Das, "Combined speed and rotor resistance estimation for speed sensorless induction motor drive using reactive power based MRAS," *Michael Faraday IET Int. Summit* 2015, Kolkata, 2015, pp. 330-335.

[34] Y. A. I. Mohamed, "A Newly Designed Instantaneous-Torque Control of Direct-Drive PMSM Servo Actuator With Improved Torque Estimation and Control Characteristics," *IEEE Trans. Ind. Electron*, vol. 54, no. 5, pp. 2864-2873, Oct. 2007.

[35] L. Zhen and L. Xu, "Sensorless field orientation control of induction machines based on a mutual MRAS scheme," *IEEE Trans. Ind. Electron*, vol. 45, no. 5, pp. 824-831, Oct. 1998.

[36] M. Tomita, T. Senjyu, S. Doki, and S. Okuma, “New sensorless control for brushless DC motors using disturbance observers and adaptive velocity estimations,” *IEEE Trans. Ind. Electron*., vol. 45, no. 2, pp. 274–282, Apr. 1998.

[37] D. Liang, J. Li, R. Qu and W. Kong, "Adaptive Second-Order Sliding-Mode Observer for PMSM Sensorless Control Considering VSI Nonlinearity," *IEEE Trans. Power Electron*., vol. 33, no. 10, pp. 8994-9004, Oct. 2018.

[38] E. Daryabeigi, H. Abootorabi Zarchi, G. Arab Markadeh, J. Soltani, and F. Blaabjerg, “Online MTPA control approach for synchronous reluctance motor drives based on emotional controller,” *IEEE Trans. Power Electron*., vol. 30, no. 4, pp. 2157 – 2166, Apr. 2015.

[39] J. Lemmens, P. Vanassche, and J. Driesen, “PMSM drive current and voltage limiting as a constraint optimal control problem,” *IEEE J. Emerg. Sel. Topics Power Electron*., vol. 3, no. 2, pp. 326 – 338, Jun. 2015.